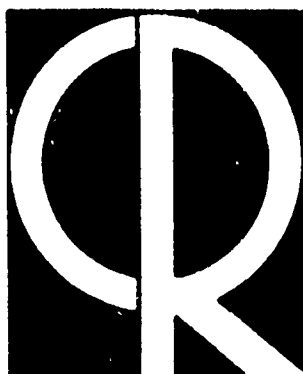


Physical Sciences Research Papers
No. 38

COPY	22 OF	131
HARD COPY		\$.
MICROFILM		\$.



DO NOT PHOTOGRAPH THIS PAGE

Apparent Sky Temperatures at Millimeter- Wave Frequencies

KARL N. WULFSBERG

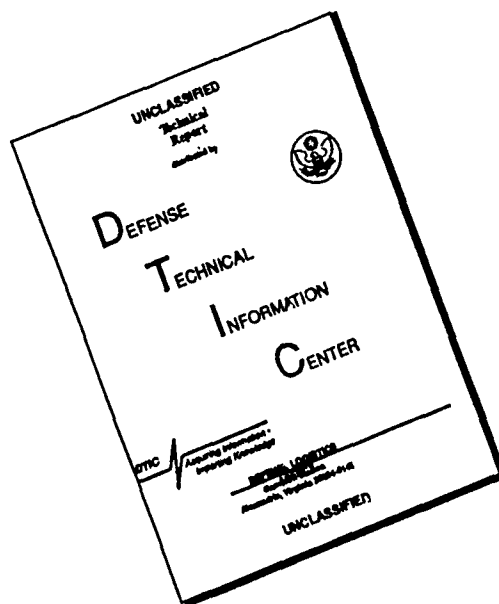
MICROWAVE PHYSICS LABORATORY PROJECT 4600

AIR FORCE CAMBRIDGE RESEARCH LABORATORIES, OFFICE OF AEROSPACE RESEARCH, UNITED STATES AIR FORCE, L.G. HANSCOM FIELD, MASS.

AD 605 813

File copy

DISCLAIMER NOTICE



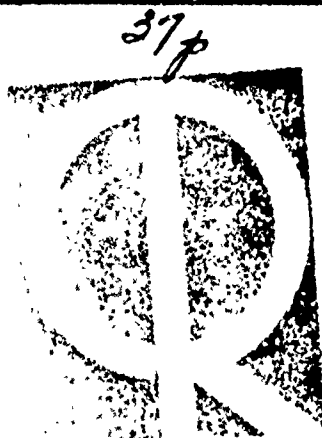
THIS DOCUMENT IS BEST
QUALITY AVAILABLE. THE COPY
FURNISHED TO DTIC CONTAINED
A SIGNIFICANT NUMBER OF
PAGES WHICH DO NOT
REPRODUCE LEGIBLY.

APCRL-44-590
JULY 1964

605 813

**Physical Sciences Research Papers
No. 38**

COPY	2	OF	3
HARD COPY	\$. 2.00		
MICROFICHE	\$. 0.50		



Apparent Sky Temperatures at Millimeter- Wave Frequencies

KARL N. WULFSBERG

I/I

MICROWAVE PHYSICS LABORATORY PROJECT 400
AIR FORCE CAMBRIDGE RESEARCH LABORATORIES, OFFICE OF AEROSPACE RESEARCH, UNITED STATES AIR FORCE, L.G. HANSCOM FIELD, MASS.

Abstract

Measurements of apparent sky temperatures taken over a one-year period at 15, 17 and 35 Gc are summarized. Sky temperature profiles for various meteorological conditions are presented as well as curves showing the percentage time distributions for various zenith angles. Such factors as absorption and radiation by oxygen and water vapor, extrapolation of the data to other geographical areas, and the relation between total attenuation of the atmosphere and sky temperature are discussed. A description of the radiometers and the calibration techniques are included.

Contents

1. INTRODUCTION	1
2. THEORETICAL CONSIDERATIONS	1
2.1 Noise Temperature Concepts	1
2.2 Atmospheric Absorption	2
2.3 Sky Temperature as a Function of Zenith Angle	3
3. SKY TEMPERATURE MEASUREMENTS	5
3.1 The Measurement Program	5
3.2 Sky Temperature Profiles	5
3.3 Effect of Antenna Beamwidth	6
3.4 Sky Temperature Distributions	8
3.5 Sky Temperatures Computed from Radiosonde Data	9
3.6 Sky Temperature Fluctuations	10
4. INSTRUMENTATION	10
4.1 Radiometers	10
4.2 Radiometer Calibration	11
4.3 Antennas	14
5. CONCLUSIONS	15
ACKNOWLEDGMENTS	29
REFERENCES	29

v / VI

Illustrations

Figure		Page
1.	Attenuation Due to Oxygen and Water Vapor at Sea Level	16
2.	Incremental Path Lengths through the Atmosphere	16
3.	Sky Temperature Profiles at 15 Gc	17
4.	Sky Temperature Profiles at 17 Gc	18
5.	Sky Temperature Profiles at 35 Gc	19
6.	Composite of Sky Temperatures and Antenna Patterns	20
7.	Sky Temperature Distributions at 15 Gc	21
8.	Sky Temperature Distributions at 17 Gc	22
9.	Sky Temperature Distributions at 35 Gc	23
10.	Seasonal Distributions of Zenith Temperatures	24
11.	Measured and Computed Sky Temperature Distributions	25
12.	Exterior View of Equipment Shelter	26
13.	Interior View of Equipment Shelter	26
14.	Radiometer Block Diagram	27
15.	Antenna Patterns at 35 and 15 Gc	28

Apparent Sky Temperatures at Millimeter-Wave Frequencies

1. INTRODUCTION

The sensitivity which can be obtained with low-noise receiving systems operating at X-band frequencies and above is often limited by the presence of noise generated in the troposphere. Both oxygen and water vapor, condensed and uncondensed, absorb and emit radiation in this part of the spectrum and account for virtually all of the sky noise. Galactic radiation, which limits sensitivity below 1 Gc, is negligible at these frequencies.

Since the noise intensity is highly weather dependent, statistical data is required on the intensity levels in order to specify the long-term performance of sensitive receiving systems. The purpose of this report is to summarize such data obtained at 15, 17 and 35 Gc over the period February 1963 to February 1964.

2. THEORETICAL CONSIDERATIONS

2.1 Noise Temperature Concepts

The noise power received from the atmosphere by an idealized directive antenna is given by

$$P_n = k T_g B \quad (1)$$

(Received for publication 4 June 1964)

where P_n is the noise power, k is Boltzmann's constant, T_s is the apparent sky temperature, or equivalent black body temperature, and B is the predetector bandwidth. If there is no precipitation in the path of the antenna, the relation between T_s and the loss through the atmosphere is

$$T_s = (1 - \alpha) T_m \quad (2)$$

where α is the fractional transmission of the atmosphere (reciprocal of the loss) and T_m is the mean absorption temperature of the atmosphere. The absorption per unit distance decreases rapidly with increasing altitude, so T_m approaches the surface temperature and normally falls in the range 250 to 290°K. Thus a fairly accurate estimate of total atmospheric losses can be obtained from sky temperature measurements.

The effect of the sky temperature on the sensitivity of receiving systems depends on the effective temperature of the system, T_r , which can be determined from the relation

$$T_r = (NF - 1) 290 \quad (3)$$

where NF is the overall system noise figure. Microwave receivers using mixers without preamplification have effective temperatures of the order of thousands of degrees and the sky temperature will have a negligible effect on sensitivity since, from Eq. (2), it cannot exceed T_m . Receivers with low-noise front ends, however, may have sufficiently low temperatures so that the sky temperatures will determine the sensitivity. A total system temperature of less than 20°K has, for example, been achieved with a mrf preamplifier at 6 Gc.

2.2 Atmospheric Absorption

The absorption of microwave radiation by atmospheric gases has been the subject of extensive investigation since World War II,¹ and is almost entirely due to the molecular absorption of oxygen and water vapor. The absorption by oxygen is due principally to a number of resonances centered at 60 Gc. Because of pressure broadening, this series of lines appears as a single broad resonance curve at normal surface pressures. The principle water vapor resonances occur at 23 Gc and at infra-red frequencies. The absorption curve, however, extends throughout the millimeter wave spectrum, again due to pressure broadening. The general shape of the curves for sea level pressure and an absolute humidity of 7.5 grams per meter³ is shown in Figure 1.

Absorption by water vapor is proportional to the water vapor density, and since the density may have seasonal variation of over 20:1, correspondingly large

variations in the absorption will occur. The absorption by oxygen, on the other hand, remains fairly constant since the oxygen density does not vary markedly with time. Given the pressure, temperature and water vapor density of a sample of the atmosphere, the attenuation per unit distance can be computed from the formulas of Van Vleck.²

Uncertainties still exist in the absorption line widths, which are pressure and temperature dependent, and thus limit the accuracy of the computed attenuation. If the vertical composition of the atmosphere is known, the total vertical attenuation can be determined by computing the attenuation of individual layers and then performing a numerical integration. The total attenuation will, of course, increase with increasing zenith angle since the path length increases. Once the absorption of the individual layers has been determined, the apparent sky temperature can be computed by summing the noise temperatures of the layers, the contribution of each layer being reduced by the attenuation between the layer and the antenna.

Since rain readily absorbs energy at these frequencies, relatively high apparent sky temperatures may result. The attenuation coefficient of rain and its frequency dependence is well established³ and thus the noise temperature due to a homogeneous rain of a given rate can be computed. Ideally the computation should be made on the basis of the absorption rather than the attenuation coefficient, which includes both absorption and scattering; the latter effect, however, is relatively small.⁴ Condensed water vapor in the form of clouds and fog is characterized by very small drop size (seldom exceeding 0.1 mm); the absorption at a given frequency depends on the total water content and is independent of drop size. Since the water concentration in clouds seldom exceeds 1 gram per meter³, the absorption and associated noise temperature is normally considerably less than that resulting from rain. The absorption coefficient of snow is small, so this type of precipitation does not contribute substantially to the total sky temperature.

2.3 Sky Temperature as a Function of Zenith Angle

Since the total path length through the atmosphere increases with zenith angle, a corresponding increase in absorption and radiation occurs. For a plane earth the path length is proportional to the secant of the zenith angle, and if the atmosphere is horizontally stratified

$$a(\phi) = a_0 \sec \phi \quad (4)$$

where a_0 is the total vertical attenuation expressed in db. The secant law is widely used in absorption calculations for the case of the spherical earth down to zenith angles of about 70 degrees. The relation can, however, also be used at larger angles with fairly good accuracy because of the increasing predominance of low altitude absorption with increasing zenith angle.

As shown in Figure 2 the path length through the first kilometer of the atmosphere is much longer than that through, for example, the 9 to 10 kilometer layer at large zenith angles. This coupled with the fact that the absorption per unit distance decreases rapidly with altitude results in a diminishing importance of higher altitude absorption at large zenith angles. A sample calculation of total atmospheric attenuation for a zenith angle of 85° and the path length associated with a $4/3$ earth radius, was found to differ from that obtained from the product of the zenith attenuation and secant 85° by less than 1%.

The apparent sky temperature at a zenith angle ϕ is given by

$$T_s(\phi) = (1 - \alpha_0^{\sec \phi}) T_m \quad (5)$$

where α_0 is the fractional transmission of the atmosphere at the zenith. To determine the dependence of T_m , the mean absorption temperature on the surface temperature and humidity, this factor was computed using the relation⁵

$$T_m = \frac{\int_0^{\tau_0} T e^{-\tau} d\tau}{1 - e^{-\tau_0}} \quad (6)$$

where T is the temperature at a given point along the ray path and τ is the absorption integrated over the ray path to the height corresponding to T . T_m was computed for various values of surface temperature and humidity at 15, 17 and 35 Gc; a surface pressure of 1013 mb was assumed. The computations revealed that T_m is essentially independent of frequency, that it is essentially linear with surface temperature and only moderately dependent on the relative humidity.

For the atmospheric model and line width constants used, the following relation holds:

$$T_m = 1.12 T_g - 50 \quad (7)$$

where T_g is the surface temperature in degrees Kelvin. The relative humidity may vary from 20 to 70% with T_m , as computed from Eq. (7), not being in error by more than 2°K . It should be noted that T_m increases slowly with zenith angle, and while T_m was computed for the zenith case only, the relation in Eq. (7) is believed useful to $\phi = 80^\circ$. Computations of sky temperature from Eqs. (5) and (7) should be limited to clear sky or thin cloud conditions, since the relations are not valid if there is appreciable absorption or scattering by condensed water in the ray path.

3. SKY TEMPERATURE MEASUREMENTS

3.1 The Measurement Program

To obtain a statistical measure of apparent sky temperatures, measurements were made on a once-a-day basis over a period of one year. Readings were taken at 12 antenna elevation positions. Sky conditions were noted at each angle and the surface temperature, pressure and relative humidity were recorded for each set of measurements. The measurements were made using conventional Dicke radiometers with pyramidal horn antennas; the equipment and calibration method are described in another section of the report. The program was carried out at the AFCRL field site at Prospect Hill, Waltham, Massachusetts, at an elevation of 480 feet.

3.2 Sky Temperature Profiles

This section of the report presents a number of curves of apparent sky temperature as a function of zenith angle under various meteorological conditions. Each curve represents a single set of data; about 15 minutes were required to obtain the data for one profile. The data for 15, 17 and 35 Gc is shown in Figures 3, 4 and 5 respectively; T_g and p refer to the surface temperature and water vapor density at the time the particular profile was taken. All the curves show a monotonic increase of sky temperature with zenith angle. Sky conditions resulting in a decrease in temperature in going from one zenith angle to a larger angle were encountered on only a few occasions.

The two lowest curves in each of Figures 3, 4 and 5 are the extremes that were measured under conditions of clear sky or cirrus clouds. The higher of the two curves is typical for hot, humid days and the lower for cold, dry days. In the former case the radiation is due principally to water vapor, and since the absolute humidity fluctuates widely in the summer months, the clear sky temperatures also varied considerably from day to day, particularly at 35 Gc. This is in contrast to winter days, where the water vapor content is so low that the oxygen emission becomes predominant, and clear sky temperatures are quite stable from day to day.

The contribution of clouds to the apparent sky temperature is a function of the total water content in the antenna path and thus depends on the cloud type and thickness. The increase in zenith temperature due to cirrus clouds, which are composed of ice crystals, was not measurable at any of the frequencies. The contribution to the zenith temperature of large fair-weather cumulus clouds ranged from 5 to 25°K at 35 Gc; an increase of only a few degrees was measured at 15 Gc. As indicated in the curves, low rain-bearing clouds result in relatively high sky temperatures.

Measurements during rain were hampered by the filming of the teflon sheets covering the apertures of the horn antennas. By drying the coverings just prior to

a measurement and by pointing the antenna away from the wind, realistic readings could be obtained except under heavy rain. During the course of the project a system was incorporated by which a compressed air stream could be directed at the coverings and proved very effective in removing the water film. Occasionally the sky temperatures changed so rapidly that the operator had difficulty in obtaining a realistic measurement.

Measurement of the temperature contribution from snow proved difficult due to the associated cloud cover. On two occasions measurements were made under conditions of light snowfall and thin cloud cover; the temperatures observed were not significantly higher than those that would be expected for a clear sky. One therefore concludes that the absorption and radiation due to snow is of relatively minor importance.

3.3 Effect of Antenna Beamwidth

Since sky temperature is a non-linear function of zenith angle, the beamwidth of the antenna will introduce an error in a measurement taken at a particular zenith angle. It would be expected that the errors would be greater at large zenith angles, where the sky temperature gradient is very high and where a significant part of the antenna beam may intercept the earth. To determine the magnitude of such errors as a function of zenith angle, theoretical sky temperature curves at 15 and 35 Gc were first computed. Typical winter conditions were assumed and the path lengths at the various angles computed on the basis of a 4/3 earth radius. Somewhat idealized two-dimensional antenna patterns were then used with the theoretical curves to determine the 'measured' sky temperatures. The computations were made using a two dimensional sum of the form⁶

$$T_s = \sum_i \bar{T}_i \left[\bar{G}_i \frac{\Delta \theta_i}{2\pi} \right] \quad (8)$$

where $\bar{G}_i \Delta \theta_i / 2\pi$ and \bar{T}_i are the average gains and temperatures, respectively, in the direction interval $\Delta \theta_i$. Figure 6 is a composite of part of the computed sky temperature curves and the antenna patterns used, with the antennas oriented at a zenith angle of 90° . The apparent ground temperatures used are typical of those measured in the winter months.

The results for 35 Gc are tabulated in Table 1.

In Table 1, Column 1 lists the computed sky temperatures and Column 2 the corresponding temperatures weighted by the antenna pattern. Despite the fact that at $\phi = 90^\circ$ the lower half of the antenna pattern intercepts the earth, the theoretical temperature is higher than that weighted by the antenna pattern, due to the high temperature gradient as ϕ approaches 90° .

TABLE 1. Measured and computed sky temperatures at 35 Gc

Zenith Angle	1	2	3	4
0°	9.6°K	9.6°K	10 - 13°K	9.6°K
30	11	11	11 - 15	11
60	19	19	19 - 23	19
70	26	26	27 - 31	27
75	34	34	35 - 40	35
80	52	53	50 - 59	51
82.5	66	68	66 - 74	65
85	88	93	91 - 100	91
87.5	132	142	138 - 157	150
90	226	213	203 - 226	---

Column 3 of Table 1 lists the extremes of 22 of the 60 profiles taken in the months of December through February. The surface temperatures varied from -10°C to $+2^{\circ}\text{C}$ and the absolute humidity from 0.6 to 3.5 grams/ m^3 ; sky conditions varied from clear sky to thin cloud cover. The greater spread in the readings at the larger zenith angles is due in part to the fact that the profiles were taken at various azimuth positions, over which the horizon varied from $\phi = 90^{\circ}$ to $\phi = 80.5^{\circ}$. The positioning accuracy of the antenna in elevation was about $\pm 0.2^{\circ}$, which also contributed to the variation in readings. The effective temperature of the earth was of course another variable, depending on foreground conditions.

The temperatures in Column 4 of Table 1 were computed from the relation $T_s(\phi) = (1 - \alpha_0 \sec \phi) T_m$. A value of 260°K was assumed for T_m and used at all angles; α_0 , the fractional transmission at the zenith, was obtained from $\alpha_0 = 1 - T_s(0)/T_m$. Some of the differences between Columns 4 and 1 of Table 1 arise from approximations made in the numerical integration used in computing the temperatures in Column 1 and in rounding off to the nearest degree; the agreement, however, is good through $\phi = 85^{\circ}$.

A similar tabulation for 15 Gc is shown in Table 2.

In Table 2, the theoretical temperatures weighted by the antenna pattern (Column 2) are considerably higher than the theoretical (Column 1) for $\phi \geq 85^{\circ}$ due to the wider beamwidth at 15 Gc and the greater difference between the theoretical temperature for $\phi = 90^{\circ}$ and for $\phi > 90^{\circ}$. The temperature extremes for 39 of the 60 profiles taken during the months December through February are listed in Column 3 of Table 2 and are seen to be in good agreement with those predicted in Column 2. The surface temperatures for the 39 profiles varied from -10° to $+8^{\circ}\text{C}$.

TABLE 2. Measured and computed sky temperatures at 15 Gc

Zenith Angle	1	2	3	4
0°	3.2°K	3.2°K	3 - 5°K	3.2°K
30	3.7	3.7	3 - 6	3.7
60	6.4	6.4	5 - 8	6.4
70	9.3	9.3	8 - 11	9.3
75	12	12	10 - 16	12.2
80	17.5	18.5	16 - 23	18
82.5	23	26	22 - 32	24
85	32	42	38 - 50	35
87.5	56	82	71 - 89	64
90	131	146	142 - 166	---

and the absolute humidity from 0.6 to 6 grams/m³. The temperatures in Column 4 of Table 2 were computed from the secant relation and again are in good agreement with those in Column 1 through $\phi = 85^\circ$.

3.1 Sky Temperature Distributions

The percentage-time distributions for the year's period at 15, 17 and 35 Gc are shown in Figures 7, 8 and 9 respectively, each curve representing 251 samples. Percentage times were computed for each degree for temperatures up to 50°K; 5° averages were used in the range 50 to 100°, and 10° averages between 100° and 300°. These points were then plotted and best-fit curves drawn. Considering the rather limited number of samples the point spread was fairly low. At 35 Gc, for example, the difference between 95% of all points plotted and the curves is less than 3%. While the scale used does not accurately describe the distributions for temperatures near the maximum, it is commensurate with the measured data. Maximum temperatures are associated with maximum rainfall rates and since heavy rain occurs over such a small percentage of the time, a more accurate distribution of sky temperatures near the maximum could probably be obtained from computations involving rainfall rate distributions rather than by period sampling.

Figure 10 shows the seasonal distributions of zenith temperatures at 15 and 35 Gc. Since oxygen absorption predominates in the winter months, the associated temperatures are more consistent from day to day than for other seasons. Ninety percent of the December - February zenith readings at 35 Gc, for example, fell within a 7° range; the corresponding range for the June - August readings was 25°. The deviations from normal temperatures and precipitation are shown in Table 3.

TABLE 3. Deviations from normal temperature and precipitation

Period	Daily Average Temperature	Precipitation
Dec - Feb	-6.8°F	+1.25"
Mar - May	+3	-2.6
Jun - Aug	+1.4	-4.71
Sep - Nov	+3.9	+2.3

Over the year's period the average daily temperature was 1.5° above normal; the total precipitation was approximately 9% below normal.

Extrapolation of the curves to other geographic areas appears difficult since it involves meteorological statistics; general trends, however, can be predicted. Two important considerations are the altitude and latitude of the location, since the mean annual precipitable water is a function of these factors only, increasing as the latitude decreases and being inversely proportional to altitude.⁷ Since the oxygen density also decreases with altitude, the total sky temperature falls off rapidly at higher elevations. A sample calculation showed a zenith temperature of 11°K at sea level decreasing to approximately 7° at 1 km and to 3° at 3 km.

The minimum zenith temperature for a particular location could be computed using a model atmosphere based on the lowest expected surface temperatures. The maximum temperature could also be computed, using the maximum rainfall rate. Determining the slope of the line joining these two extremes of the distribution would be difficult, however, since it involves the statistics of temperature, humidity, cloud cover and rainfall. In general, the more stable the yearly weather pattern, the steeper the slope. Once the zenith temperature distribution is known, fairly accurate distributions for zenith angles of 85° or less can be readily determined from the secant relation of Eq. (5). Figure 11 shows a comparison of measured and computed distributions at 35 Gc; the computation method was similar to that used to determine the temperatures in Column 4 of Table 1.

3.5 Sky Temperatures Computed from Radiosonde Data

During the course of the measurement program, several sky temperature profiles were taken at the time of radiosonde launchings from Hanscom Field. Zenith sky temperatures were computed from the radiosonde data with the aid of a digital computer and were in close agreement with measured values. A discussion of the computational method, the line-width constants used and other theoretical considerations will be included in a future report to be authored by V. Falcone, AFCL.

3.6 Sky Temperature Fluctuations

Since small-scale fluctuations in the apparent sky temperature may degrade the performance of sensitive microwave radiometers, the amplitude distribution of such fluctuations is of considerable interest to radio astronomers. Sky temperature fluctuations imply a fluctuation in atmospheric attenuation, so a corresponding scintillation in signals transmitted through the atmosphere would be expected. It has been mentioned that clouds passing through the antenna path can produce significant increases in the sky temperature, the magnitude depending on the total water content and the frequency of operation. Clear sky temperature fluctuations are presumably due to variations in the water vapor content in the path of the antenna. The relatively large fluctuations encountered in rain are of lesser concern since radio astronomy measurements are not normally made under such conditions.

To determine the feasibility of measuring temperature fluctuations, the output of the 15 Gc radiometer was recorded for a total of 6 hours during the month of January; the antenna zenith angle was 30° and sky conditions varied from clear to moderately heavy cloud cover. Peak fluctuations of the radiometer itself, as determined by replacing the antenna with a matched load, was 0.8°K with an integration time of 8 seconds. Peak sky temperature fluctuations exceeded this value less than 4% of the time. Thus a considerably more sensitive radiometer is required to obtain meaningful statistics of the fluctuations, particularly if fine-grain data is desired, which implies a shorter integration time.

4. INSTRUMENTATION

Two radiometers were employed in the measurement program, one operating at 35 Gc and the other time shared between 15 and 17 Gc; the frequency change merely required retuning the local oscillator and adjusting the ferrite switch drive current. The radiometer front ends were mounted on the antenna elevation mount and connected directly to the horn antennas, thus eliminating rotary joints and transmission line losses. The equipment was housed in a maintenance shelter of World War II vintage which was mounted on a rotating platform formerly used with an experimental UHF antenna. Measurements could thus be made at any elevation or azimuth angle. Exterior and interior views of the shelter are shown in Figures 12 and 13.

4.1 Radiometers

The two radiometers, of the switched load type, were designed and constructed in the laboratory. The basic circuits of the two radiometers were identical; a block diagram is shown in Figure 14. The principle of operation is as follows. The ferrite switch, or modulator, alternately samples the noise output of the directional

coupler and the noise produced by a load at ambient temperature T_0 . If the two levels are not equal, the input to the mixer appears as noise amplitude-modulated at the switching frequency. The detected IF amplifier output is then a noisy square wave. After passing through the filter amplifier, the 30 cps signal is applied to the synchronous detector. The fluctuating d-c output is then integrated, amplified and applied to a meter or recorder. In practice the precision attenuator is adjusted for an output meter null, in which case the antenna noise temperature plus that injected from the noise source is equal to the load temperature T_0 . The injected noise temperature is determined from the attenuator setting and since T_0 is known, the antenna temperature can be computed.

The choice of the IF amplifier center frequency is important in the design of radiometers because of possible interference from signals falling in the IF passband. As the result of a frequency survey conducted at the site, 125 Mcps was chosen as the center frequency. Interference at this frequency was in general limited to transmissions from nearby aircraft. An audio monitor following the IF detector proved useful in detecting interference, and measurements were suspended during these brief periods.

While multiple and submultiples of the power line frequency are usually avoided as radiometer switching frequencies, no difficulty was experienced in using half the line frequency. Although 60 cps hum is present at the input to the synchronous detector, it produces no d-c component at the output. Good frequency stability of both the switching frequency and the narrow band filter is required to insure that the phase of the signal applied to the synchronous detector does not vary excessively. Locking a multivibrator to half the line frequency insured a stable switching frequency. An L-C filter was employed in the 30 cps filter amplifier and little difficulty was experienced with phase drift.

The minimum increment of temperature detectable by a radiometer is determined by output noise fluctuations due to the radiometer itself, and is a function of system noise figure, bandwidth and integration time. The peak fluctuations of the radiometers used were measured by replacing the antennas with matched loads and applying the outputs to a calibrated chart recorder. A peak fluctuation of 0.8°K was measured at 15 Gc, 0.9°K at 17 Gc and 1.8°K at 35 Gc. An integration time of 8 seconds was used, which was the value employed for all the sky temperature measurements.

4.2 Radiometer Calibration

As described previously, temperature readings were taken by adding sufficient noise to that received by the antenna to produce an output null. Under these conditions $T_a = T_0 - T_n'$, where T_a is the antenna temperature, T_0 is the temperature of the reference load and T_n' is the added temperature. Using the derivation by Hunt⁸ it may be shown that

$$T_a = T_o - \frac{K}{L_n} \quad (9)$$

where L_n is the setting of the precision attenuator and

$$K = \frac{L_1 C_2}{L_2 C_1} (T_n - T_o) \quad (10)$$

where L_1 is the loss between the antenna terminal and the directional coupler, L_2 is the loss between the noise source and the coupler, including the fixed insertion loss of the attenuator, C_1 and C_2 are the coupler coefficients and T_n is the temperature of the noise source. It should be noted that these relations assume that all loss components are at a temperature T_o .

There are two methods for determining the K factor. If the antenna is replaced by a matched load immersed in a liquid of known temperature and L_n adjusted for a null, the K factor may be computed directly from Eq. (9). The second method requires sky temperature readings at the zenith and 60° from the zenith. If one assumes that the temperature at 60° is twice that at the zenith, the K factor can be computed from the relation

$$K = T_o \frac{L_a L_b}{2L_b - L_a} \quad (11)$$

where L_a is the attenuator setting for a null at the zenith and L_b the setting at 60° . The second method has an advantage in that the small ohmic loss of the antenna is included in the calibration. It also provides a convenient running check of the K factor with no disassembly of the front end.

From Eq. (5) the relation between the zenith temperature $T_s(0)$ and that at 60° , $T_s(60)$ is

$$\frac{T_s(60)}{T_s(0)} = \frac{(1 - \alpha_o^2) T_m(60)}{(1 - \alpha_o) T_m(0)} \quad (12)$$

Assuming $T_m(0) = T_m(60)$,

$$\frac{T_s(60)}{T_s(0)} = 1 + \alpha_o$$

And since $\alpha_o = 1 - \frac{T_s(0)}{T_m}$,

$$\frac{T_s(60)}{T_s(0)} = 2 - \frac{T_s(0)}{T_m} \quad (13)$$

From Eq. (13) it is seen that the calibration accuracy decreases with increasing zenith temperature.

Certain precautions were necessary for a consistent calibration, or K factor. It was found that even slight flexing at some waveguide joints, particularly at the directional coupler, produced a noticeable change in calibration. Since the entire waveguide structure moved with the antenna, it was necessary to provide very solid mountings for all waveguide components. The frequency of the local oscillator was carefully monitored, since the calibration was found to be quite frequency sensitive. The gas discharge noise-source current was also monitored. An important problem arose in the accurate determination of the output meter reading corresponding to a balance or null condition. Since the meter was connected to a d-c amplifier it was subject to drift, and periodic checks of the null reading were necessary. To obtain a null condition, the antenna was replaced with a load at a temperature T_o and the noise source turned off. Under these conditions the meter reading was found to be a function of the ferrite switch current, being particularly critical in the 35 Gc system. This offset is believed due to local oscillator noise being reflected into the mixer by the ferrite switch.

Since the VSWR of the switch is a function of the drive current, the reflected noise is modulated at the switching frequency with a resultant meter deflection. The switch current required to give the same meter deflection as that obtained when the input to the IF amplifier was disconnected was noted, and subsequent measurements of the VSWR of the switch at this current and in the 'off' condition were found to be approximately equal. During temperature measurements the switch currents were carefully monitored, and the meter deflection corresponding to a null condition was obtained by simply disconnecting the inputs to the IF amplifiers.

Under conditions of clear sky or cirrus clouds and zenith temperatures less than 12 to 13°K, temperatures were computed from a K factor computed from Eq. (11). Under other conditions temperatures were obtained from calibration charts based on average K factors. The variation in the individual K factors was less than $\pm 1.5\%$ over the course of months.

The accuracy to which measurements could be made is rather difficult to assess since it involves both the attenuator accuracy and the minimum detectable temperature. If the stated accuracy of the attenuator (0.1 db) is considered in a K factor calculation, excessive errors result. The important factor in the calculation,

however, is the difference in the two attenuator readings, and since this is a small fraction of a decibel, it is reasonable to assume that the readings were good to 0.01 db, which is about the accuracy to which the attenuator could be read. This assumption leads to possible errors of about 2°K at the lower temperatures. Several measurements using a load immersed in a dry ice-acetone mixture and in liquid nitrogen were within 3°K of the bath temperatures; readings from most of the clear-sky winter profiles also fall within this tolerance when compared to those computed from the secant law for $\phi \leq 75^\circ$. Measurement accuracy for $\phi > 75^\circ$ degrades due to the effect of the antenna beamwidth and the inaccuracy in antenna positioning.

4.3 Antennas

A very important factor in the measurement of sky temperatures is the characteristics of the antenna used. Spillover and sidelobes intercepting the relatively warm earth can produce sizable contributions to the antenna temperature and thus must be minimized. High directivity is required for good resolution at large zenith angles since the sky temperature gradient is high at these angles. Another requisite is low VSWR. Since the antenna is essentially terminated in an ambient load, it radiates noise at this temperature and a poor match could result in an apparent temperature due to reflected noise.

Optimum pyramidal horns were chosen for the measurements since they meet these requirements quite well, are fairly simple to design and fabricate, and could be readily connected to the radiometers directly. H-plane sidelobes are inherently very low. Thus by orienting the horns so the H-plane was in the vertical, the pick-up of earth radiation was negligible except at large zenith angles. The E-plane sidelobes were not troublesome since the sky temperature is normally quite constant over the azimuth angle subtended by these sidelobes. Horn antennas have a disadvantage in that a weather-tight covering is required. Also, since doubling the gain of such antennas requires doubling the length, they have a rather definite maximum practicable gain.

The horns were fabricated of aluminum, dip brazed and iridized; their overall length was 6 feet. Thin teflon sheets were used to cover the horn apertures; the losses introduced by the coverings were very low and the noise contribution was not measurable. Dry air at low pressure prevented condensation on the inner surface of the teflon.

The antenna characteristics are tabulated below:

<u>Frequency</u>	<u>Gain</u>	<u>Beamwidth</u>	<u>VSWR</u>
15 Gc	30.6 db	6°	1.01
35 Gc	34.9 db	3°	1.00

E- and H-plane patterns at 15 and 35 Gc are shown in Figure 15.

5. CONCLUSIONS

From the results of the measurement program, it is evident that noise generated in the troposphere can seriously degrade the sensitivity of receiving systems operating above X-band and employing low-noise front ends. The problem is particularly acute as the antenna position angle approaches the horizon. During the year's period, zenith sky temperatures of 7, 8 and 17 degrees Kelvin were exceeded 50% of the time at 15, 17 and 35 Gc, respectively; at a zenith angle of 85° the corresponding temperatures were 58, 75 and 138 degrees. Clear sky zenith temperatures of 3, 4 and 10 degrees were typical for cold, dry days at 15, 17 and 35 Gc, respectively; for hot, humid days the corresponding temperatures were 8, 12 and 28 degrees. The temperature contribution of cirrus clouds was found to be negligible at all frequencies. The increase in zenith temperature due to large fair-weather cumulus clouds ranged from 5 to 25 degrees at 35 Gc; an increase of only a few degrees was measured at 15 Gc. Rain and rain-bearing clouds produced relatively high sky temperatures.

Extrapolation of the statistical data to other geographical areas appears difficult since it involves the statistics of local temperature, humidity, cloud cover and rainfall rate. Once the zenith temperature distribution is known, the distributions for other angles can readily be computed from the secant law.

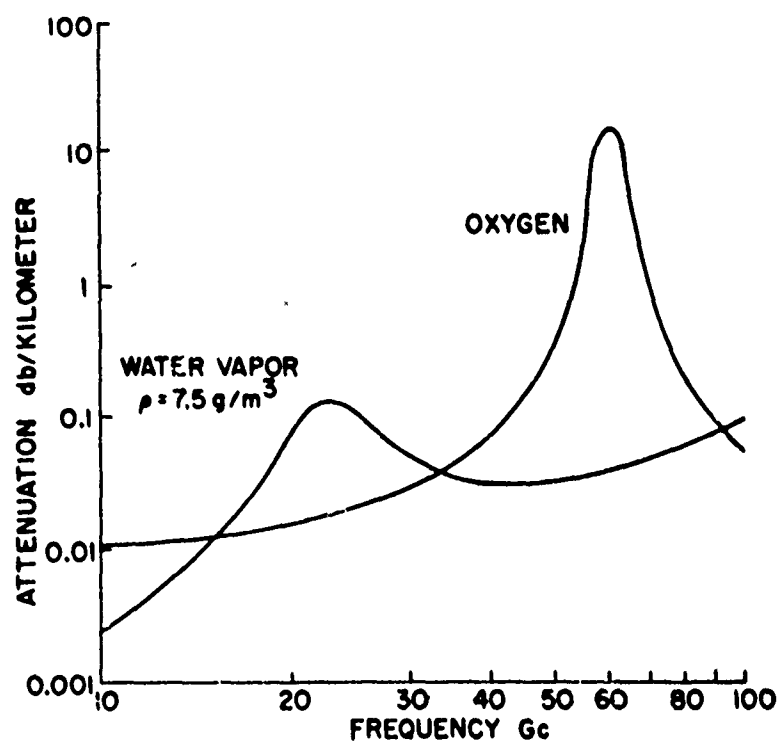


Figure 1. Attenuation Due to Oxygen and Water Vapor at Sea Level

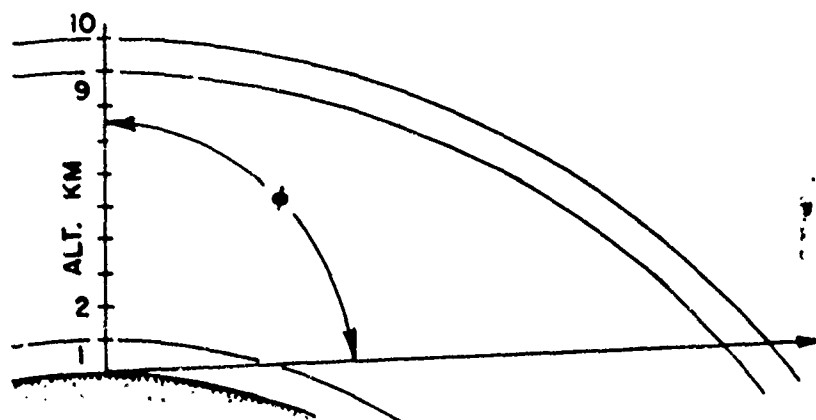


Figure 2. Incremental Path Lengths through the Atmosphere

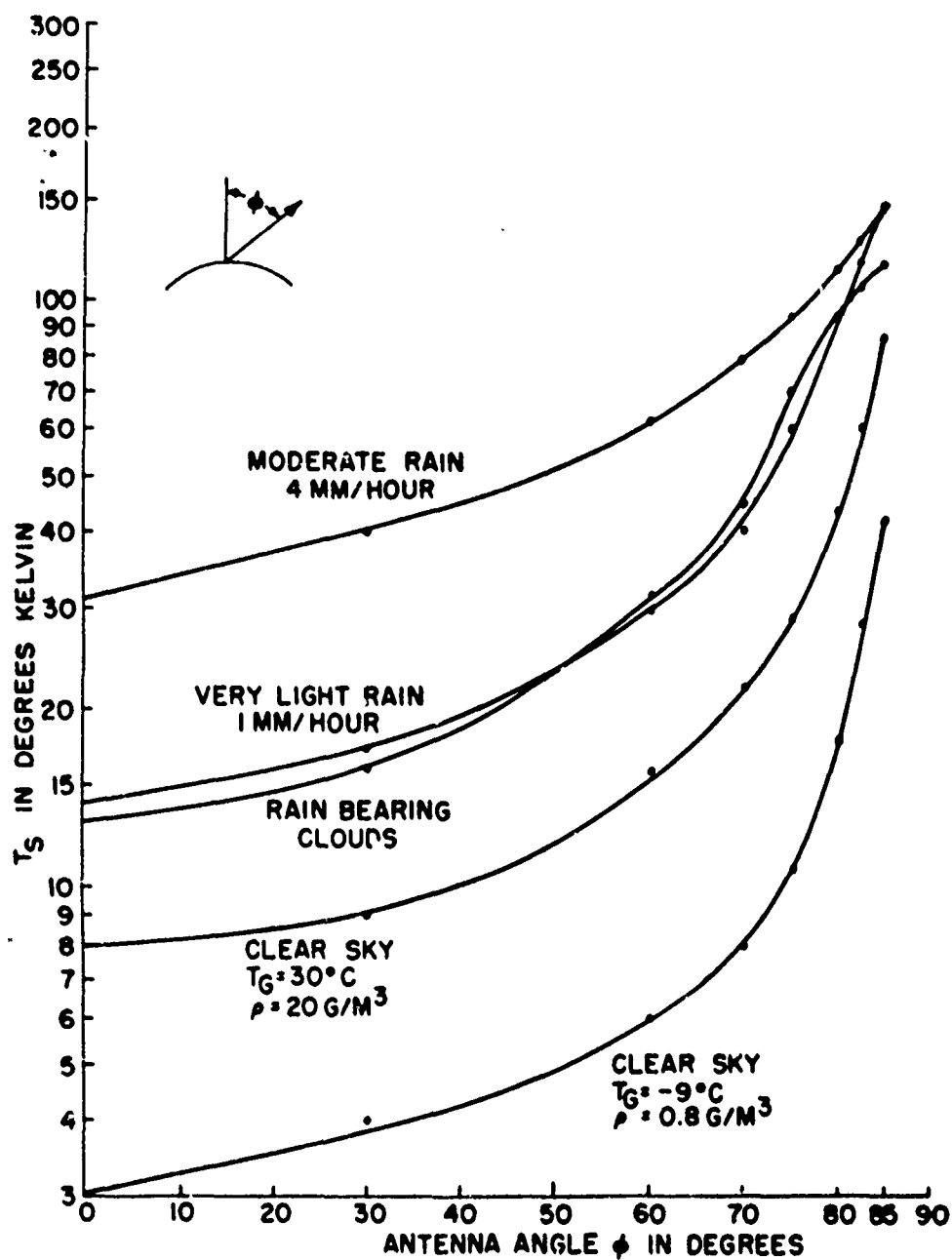


Figure 3. Sky Temperature Profiles at 15 Gc

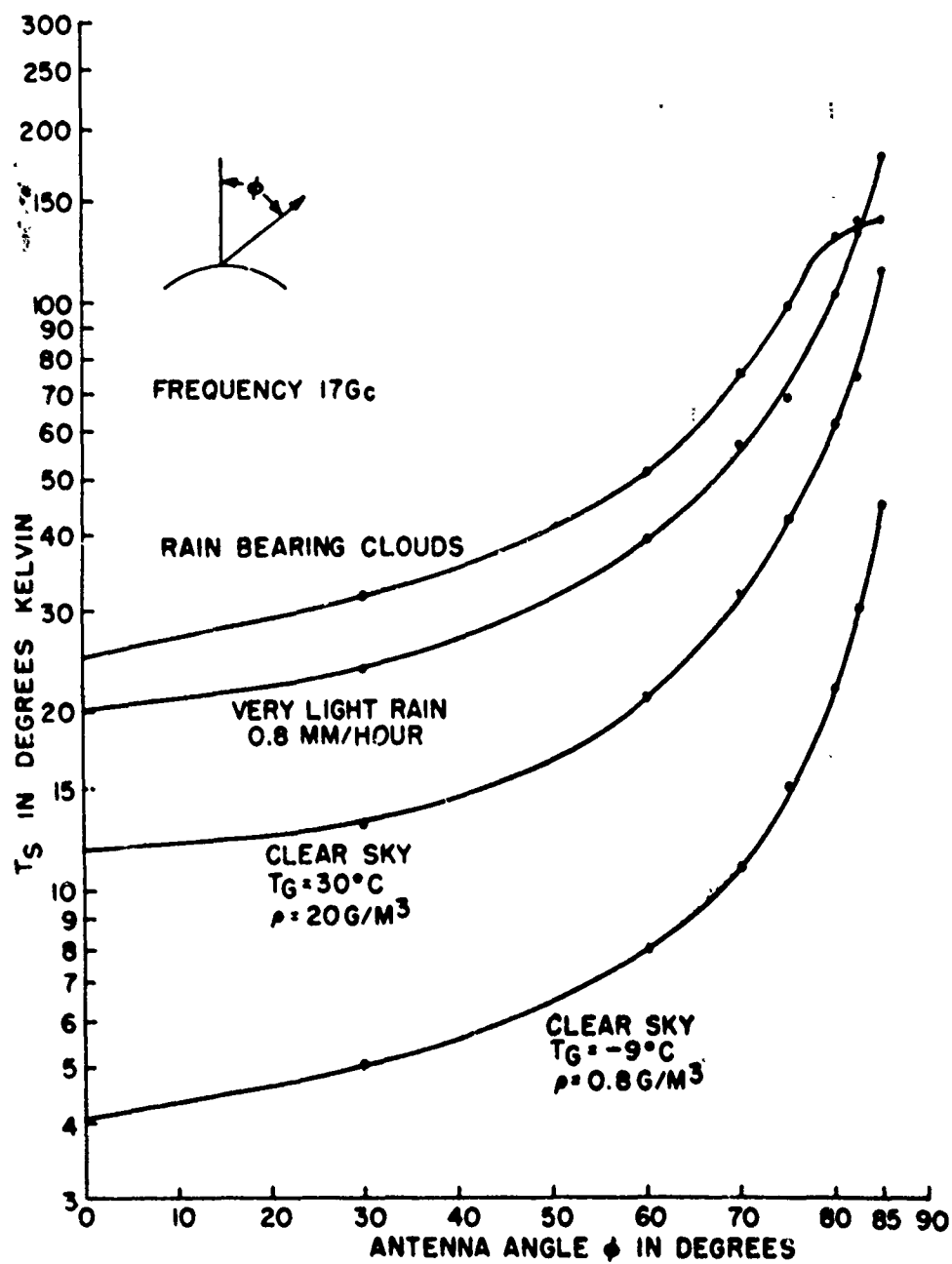


Figure 4. Sky Temperature Profiles at 17 Gc

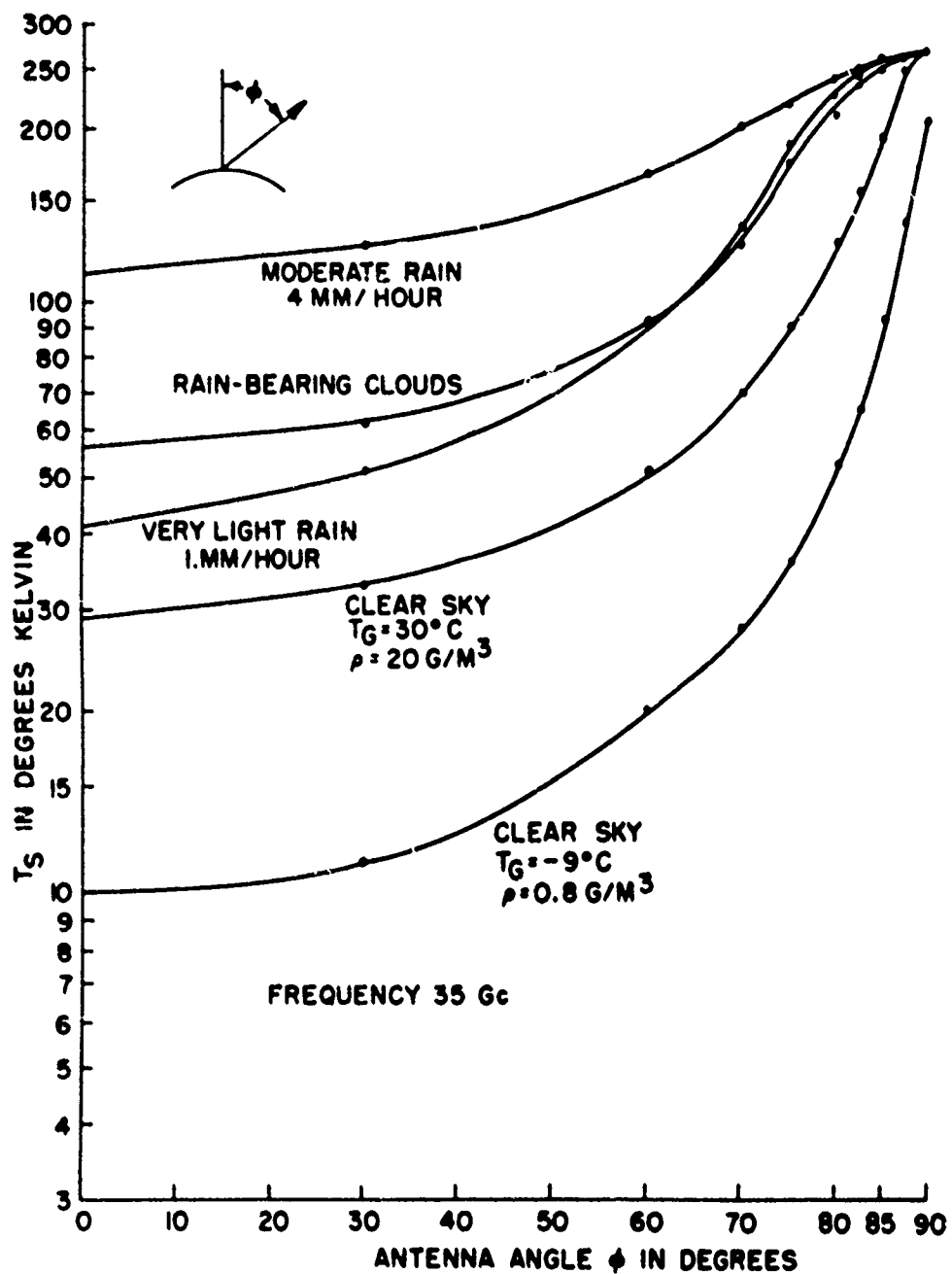


Figure 5. Sky Temperature Profiles at 35 Gc

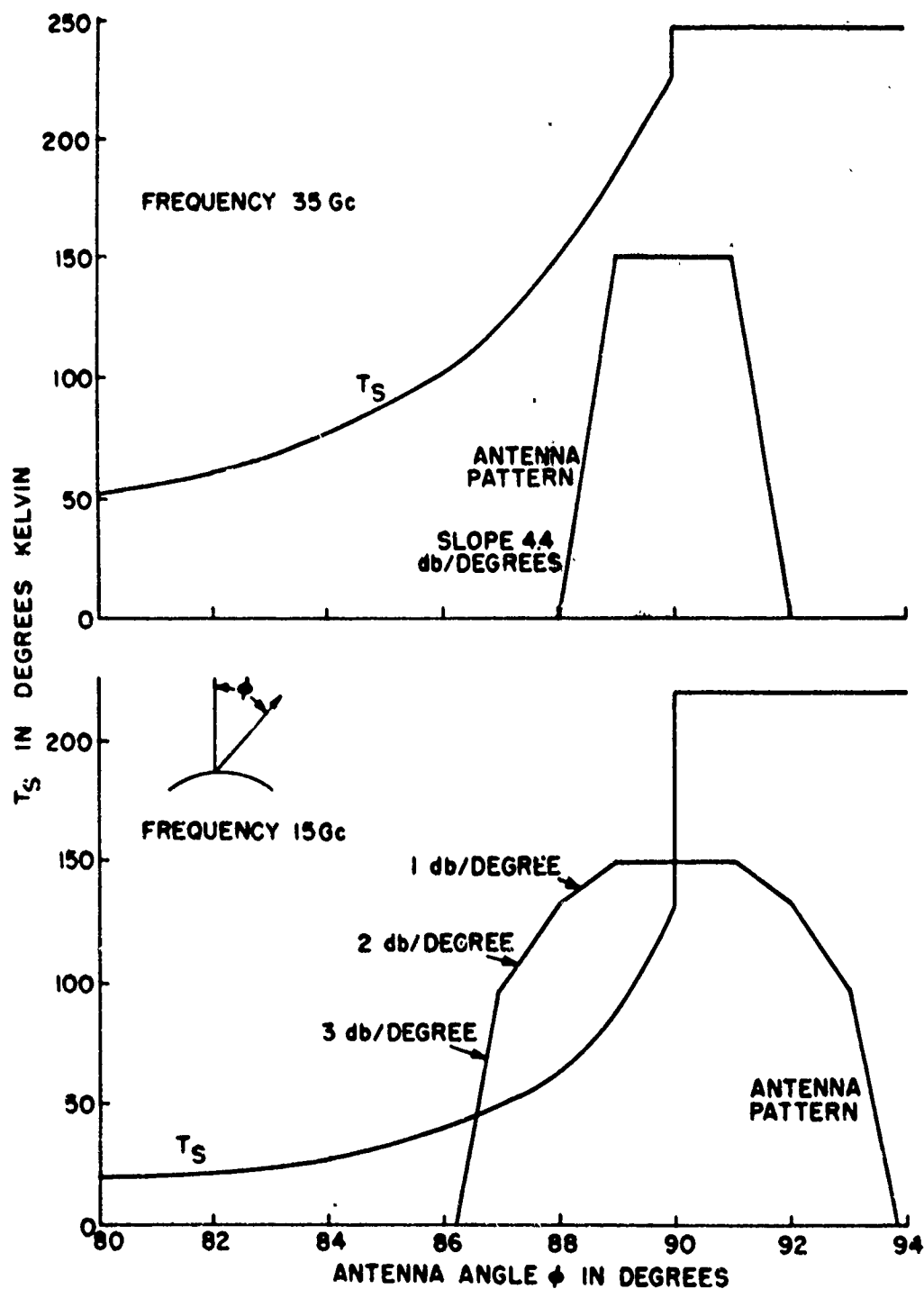


Figure 6. Composite of Sky Temperatures and Antenna Patterns

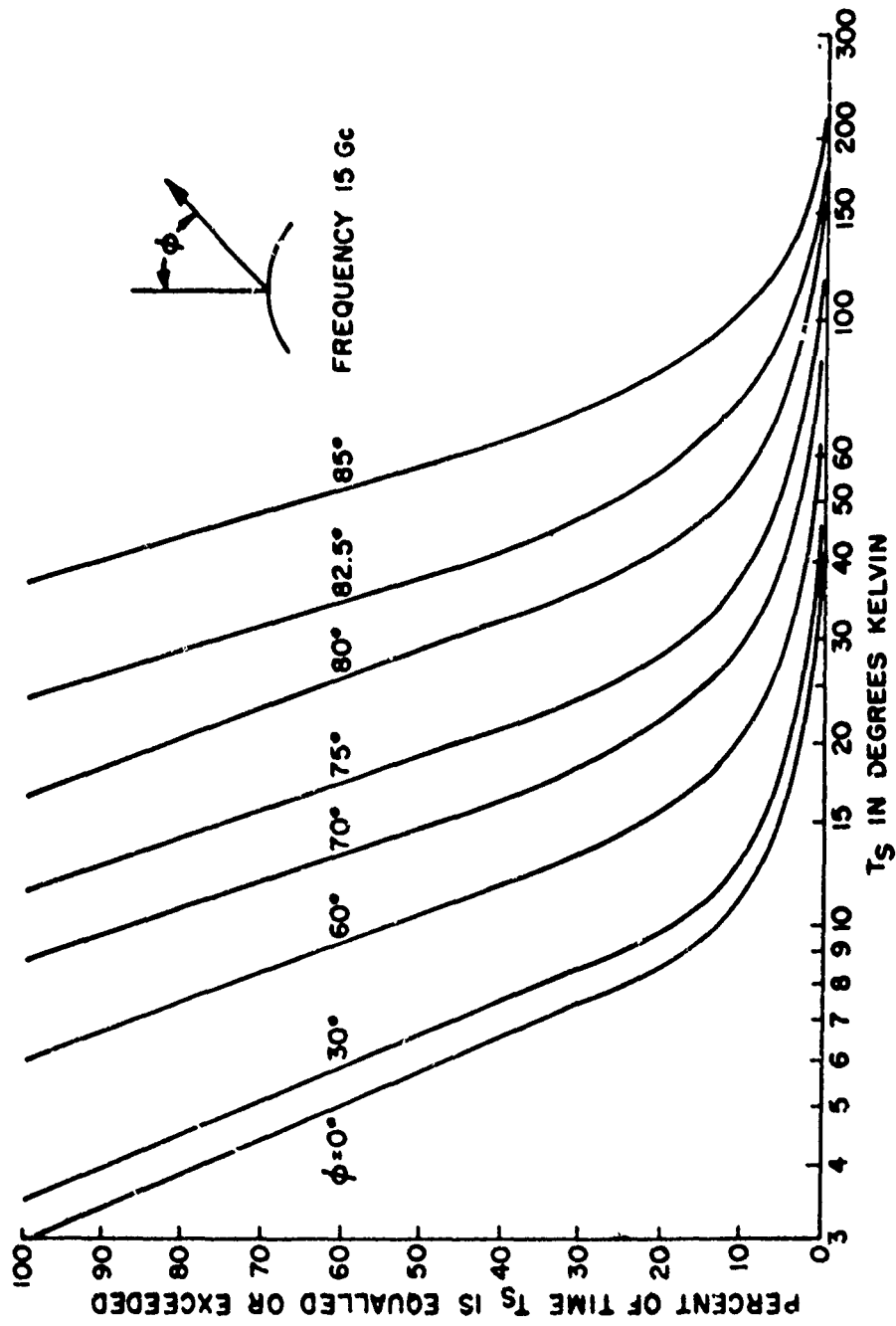


Figure 7. Sky Temperature Distributions at 15 Gc

X

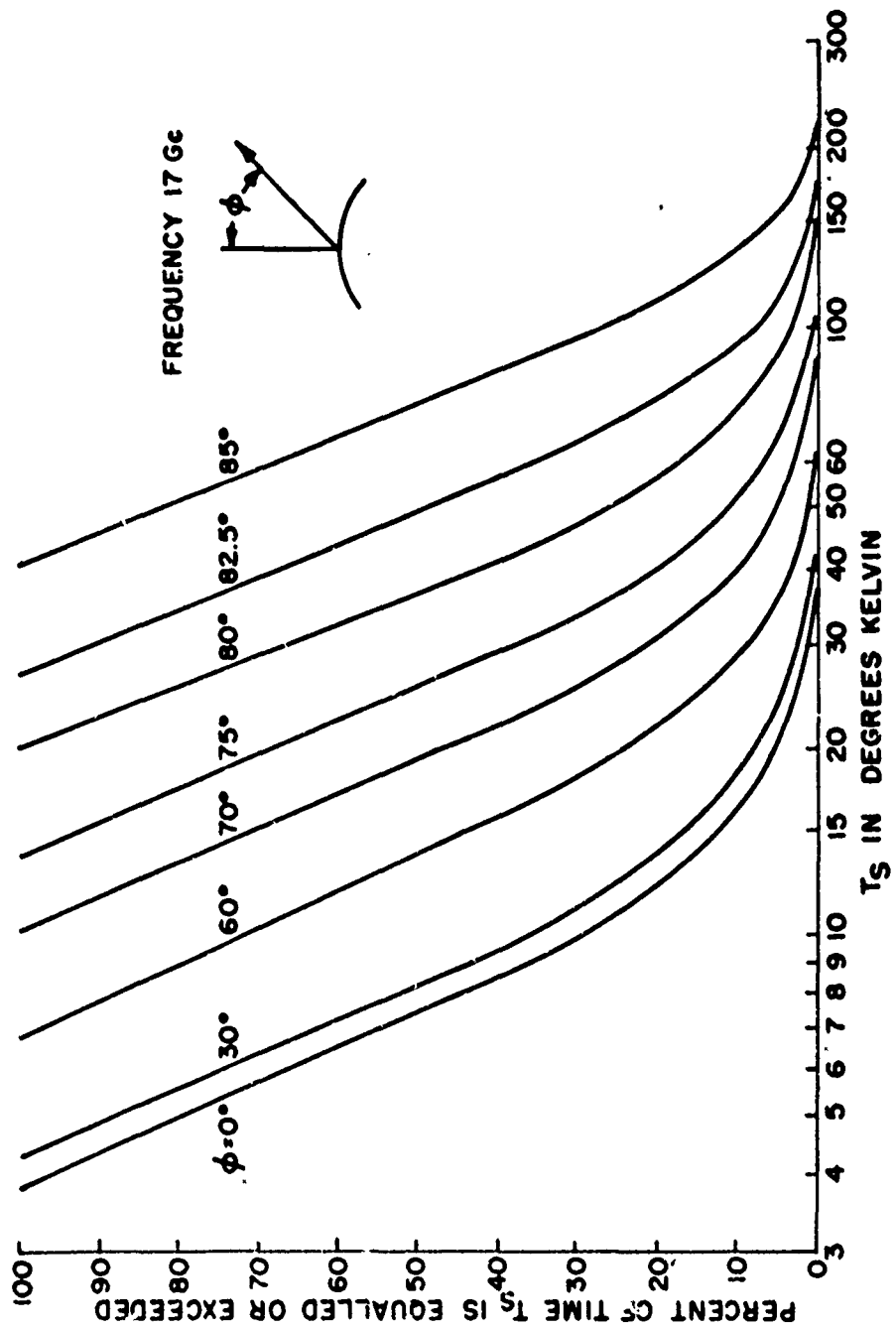


Figure 8. Sky Temperature Distributions at 17 Gc

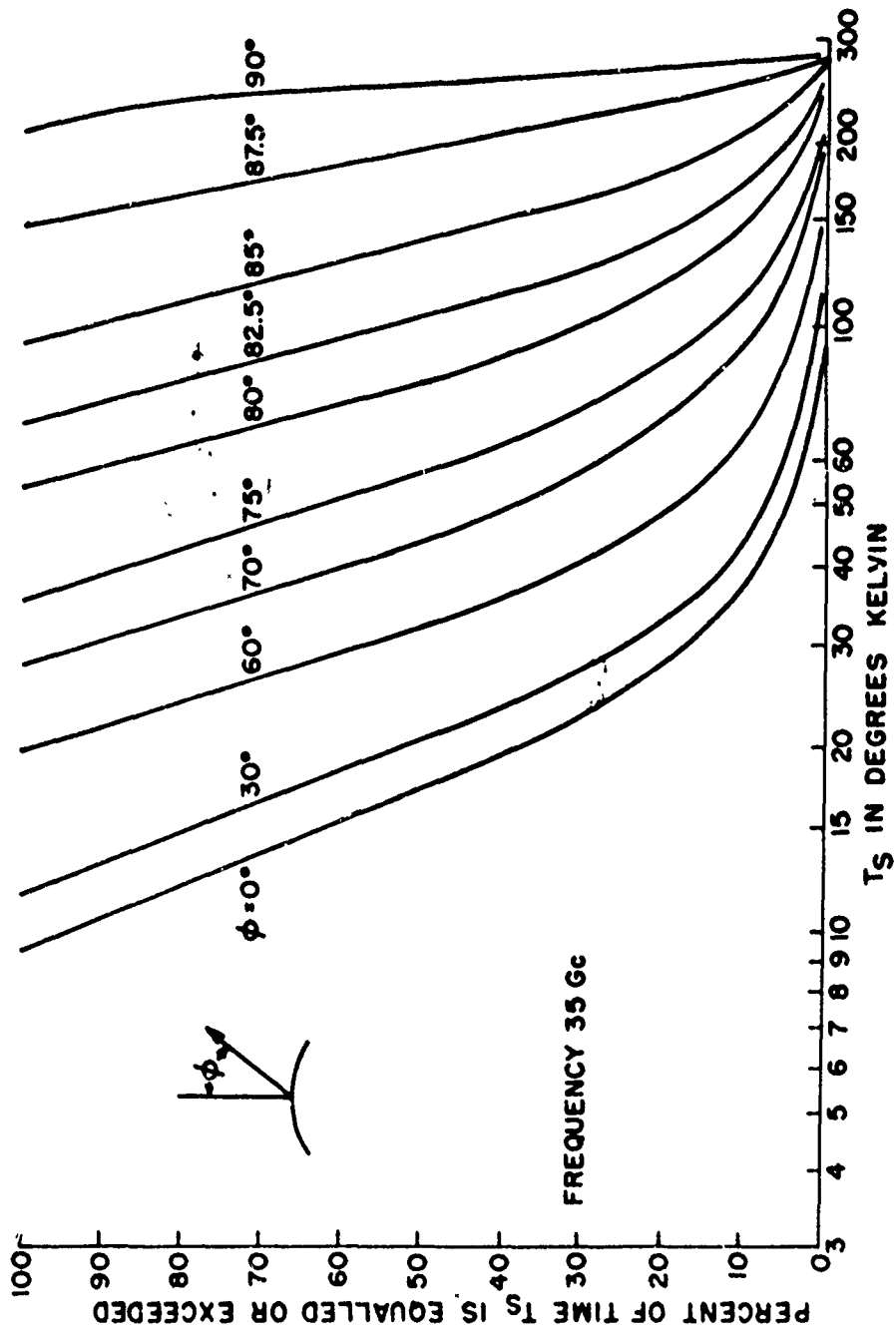


Figure 9. Sky Temperature Distributions at 35 Gc

23

23

1/2

FRAMES

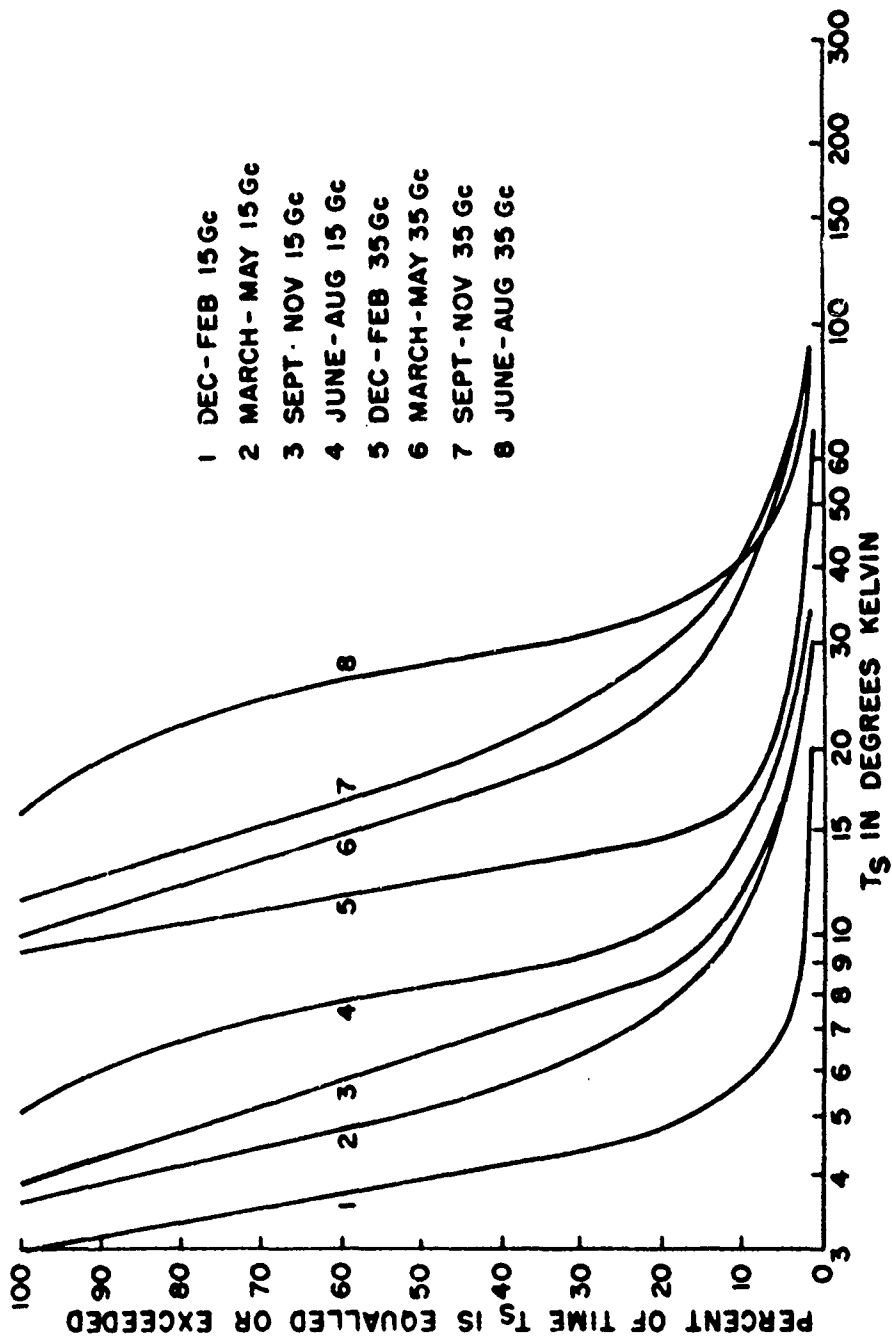


Figure 10. Seasonal Distributions of Zenith Temperatures

24

24

1/2
FRAMES

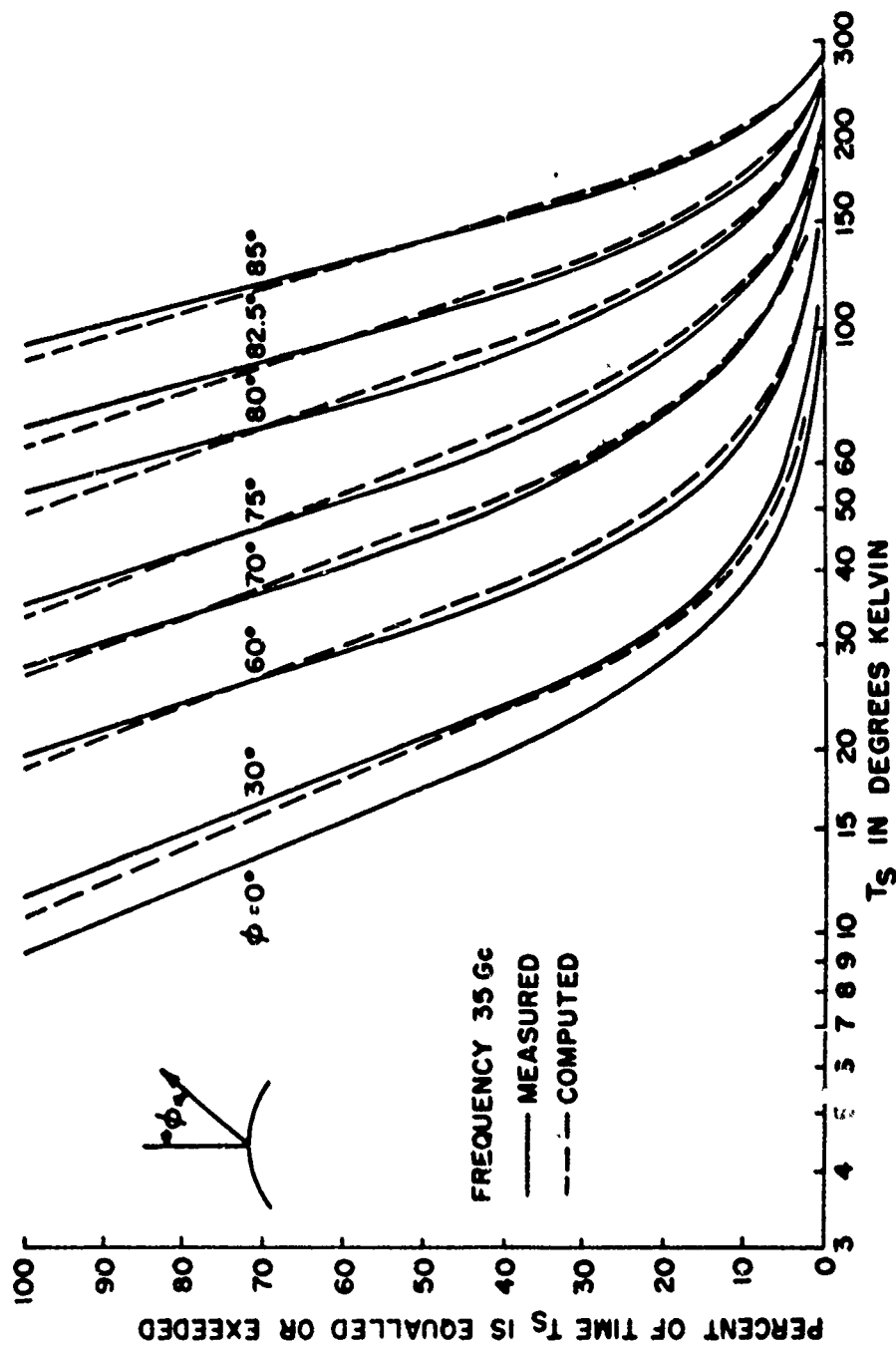


Figure 11. Measured and Computed Sky Temperature Distributions

25

25

X

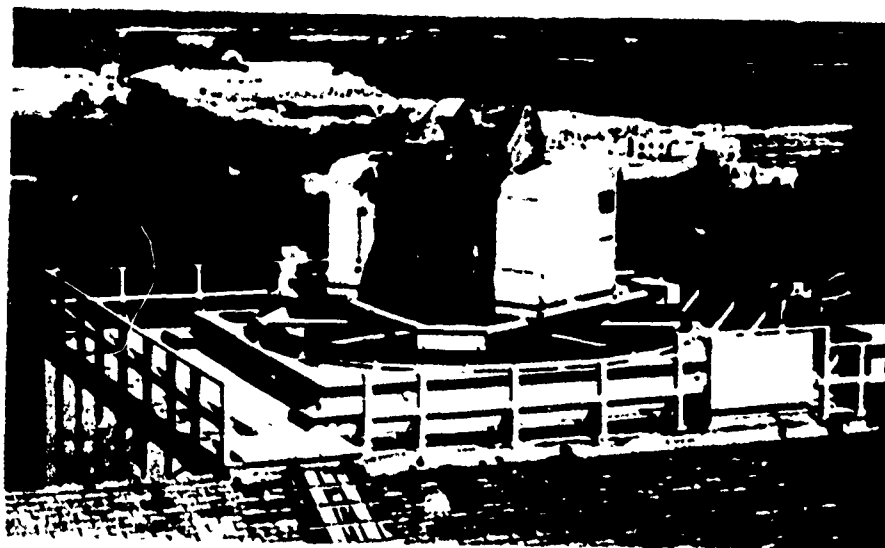


Figure 12. Exterior View of Equipment Shelter

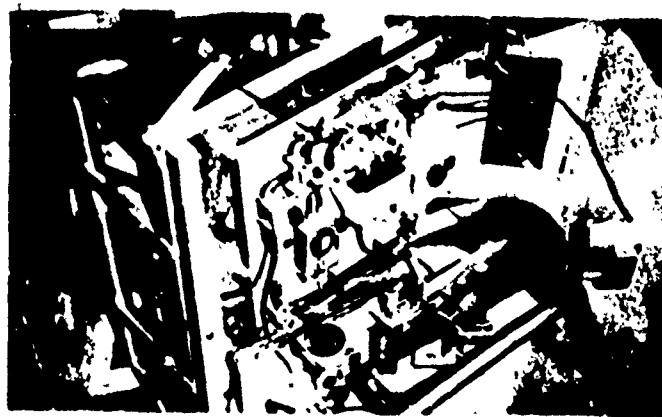


Figure 13. Interior View of Equipment Shelter

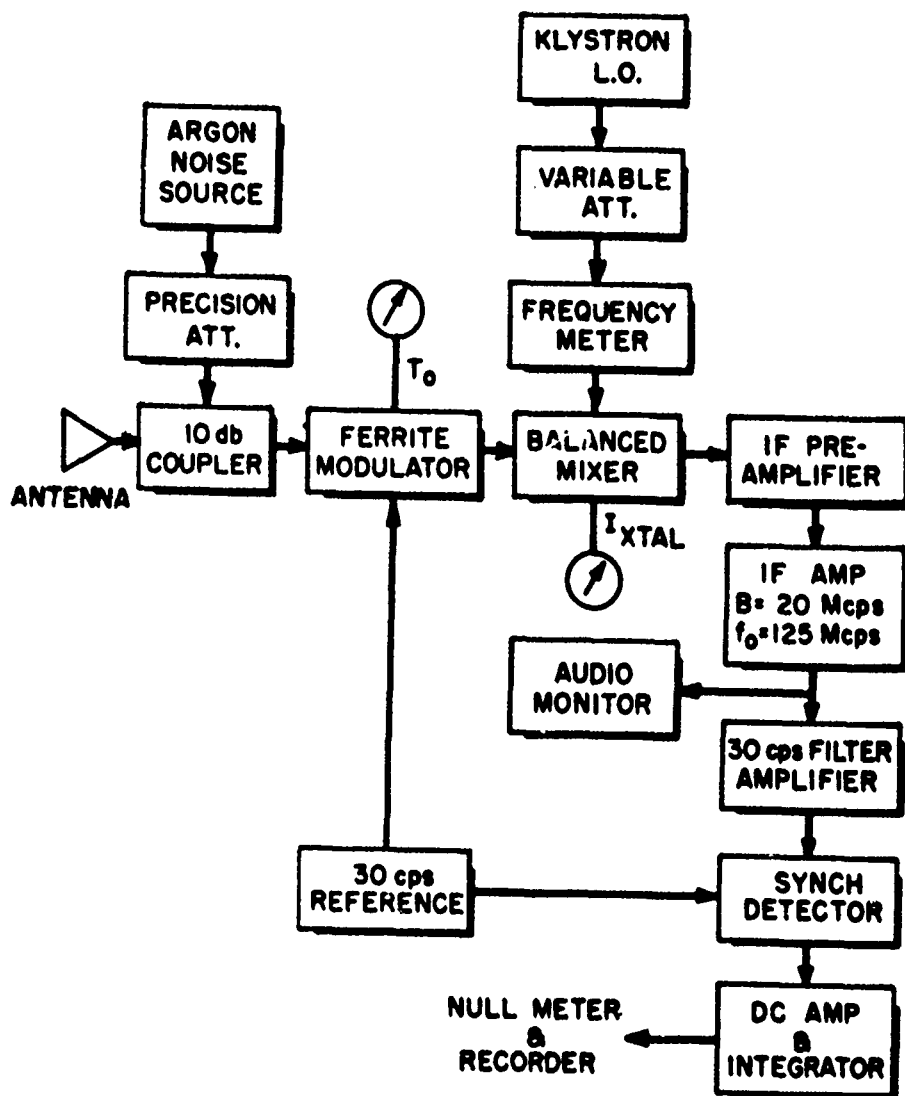


Figure 14. Radiometer Block Diagram

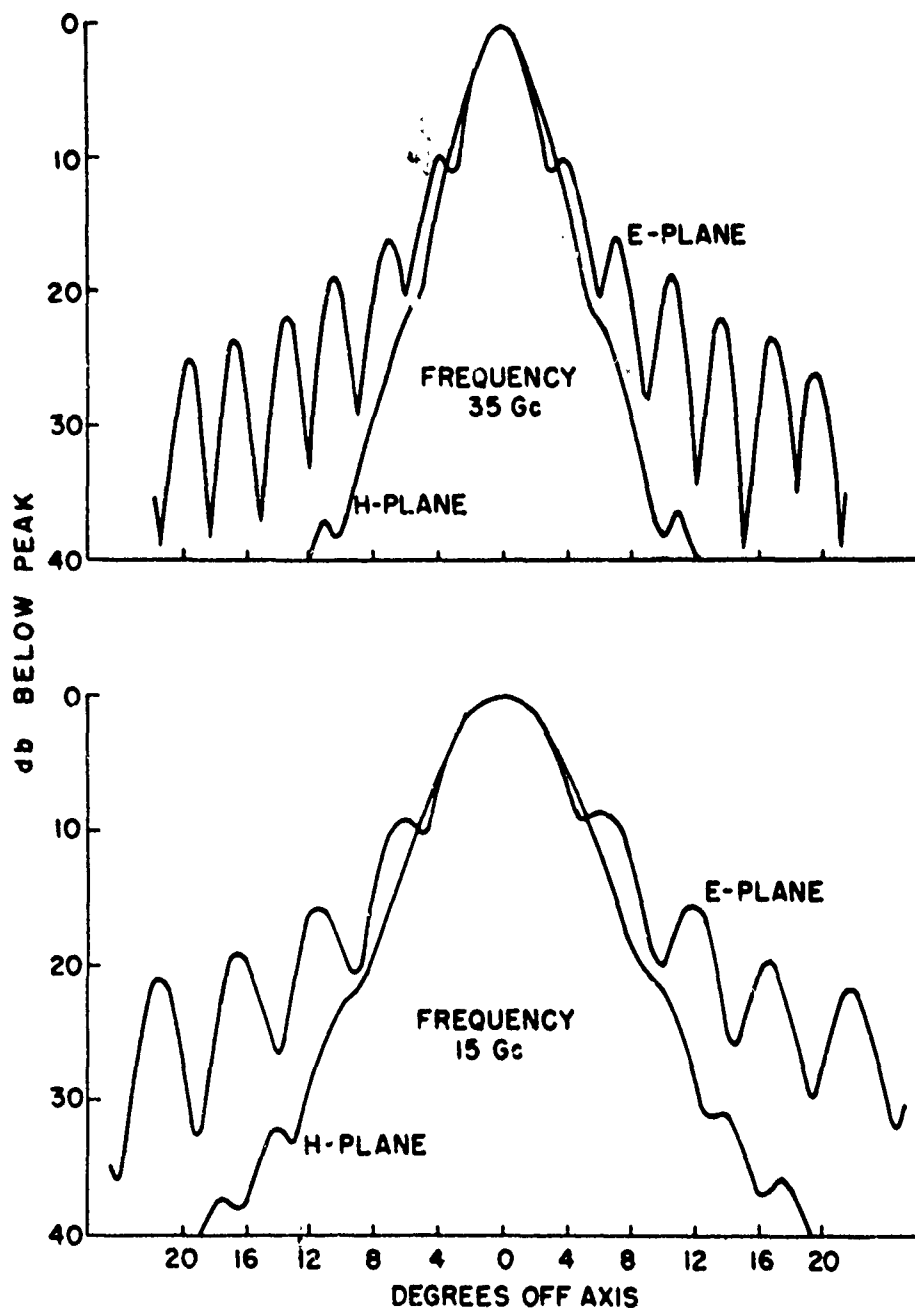


Figure 15. Antenna Patterns at 35 and 15 Gc

Acknowledgments

Because of the in-house nature of this program, a number of laboratory personnel contributed to both program and equipment design. Particular credit is due Leonard Herrick, who built and tested much of the equipment, made most of the measurements and assisted in the data reduction. Arthur Holmes lent valuable assistance during the course of the program. Data on the mean absorption temperature of the atmosphere was furnished by Vincent Falcone.

References

1. E. S. Rosenblum, Atmospheric absorption of 10-400 kMcps radiation, Summary and Bibliography to 1961, Microwave Journal 91-96, March 1961.
2. J. H. Van Vleck, Propagation of Short Radio Waves, 13, MIT Rad. Lab. Ser.
3. K. L. S. Gunn and T. W. R. East, Microwave properties of precipitation particles, Q. J. Roy. Meteor. Soc. 80:552-545, Oct 1954.
4. D. C. Hogg and R. A. Semplak, Estimated sky temperatures due to rain for the microwave band, Proc. IEEE 51:498-500, March 1963.
5. M. Schulkin, Determination of microwave atmospheric absorption using extra-terrestrial sources. NRL Report 3843, Oct 1951.
6. R. Forward and F. Richey, Effects of external noise on radar performance, Microwave Journal 3 (No. 12), Dec 1960.
7. F. Drake, NRAO radiometric experiments. The Application of Passive Microwave Technology to Satellite Meteorology: A Symposium. Memorandum RM-3401-NASA, August 1963.
8. S. Hunt, A. Orange and K. Glick, High Altitude X-Band Noise Measurements, AFCRL-63-87, April 1963.

PHYSICAL SCIENCES RESEARCH PAPERS

- No. 1. Central-Force Laws for an Elliptic Orbit, *Kurt Toman, March 1964 (REPRINT).*
- No. 2. Structure of 10, 10-Dibromonanthrene, *J. Silverman, N. F. Yannoni, February 1964 (REPRINT).*
- No. 3. Ion Dissociation in the Drift Tube of a Time-of-Flight Mass Spectrometer: V. Analytic Solutions of the Flight-Time Shift Equation, *W. W. Hunt, Jr., M. J. Kennedy, February 1964.*
- No. 4. Asymptotic Form of the Electron Capture Cross Section in the Impulse Approximation, *R. A. Mapleton, March 1964 (REPRINT).*
- No. 5. Intelligibility of Excerpts From Fluent Speech: Effects of Rate of Utterance and Duration of Excerpt, *J. M. Pickett, Irwin Pollack, March 1964 (REPRINT).*
- No. 6. Back-Scatter by Dielectric Spheres With and Without Metal Caps, *David Atlas, Kenneth M. Glover, March 1964 (REPRINT).*
- No. 7. An Adaptive Filter for the Design of Ionospheric Disturbance Detectors (U), *Richard D. Smallwood, 1/Lt, USAF, February 1964 (SECRET).*
- No. 8. The Nonlinear Interaction of an Electromagnetic Wave With a Time-Dependent Plasma Medium, *Robert J. Papa, April 1964.*
- No. 9. Drastic Reduction of Warm-up Rate Within a Dewar System by Helium Desorption, *Peter D. Gianino, January 1964.*
- No. 10. The Antipodal Image of an Electromagnetic Source, *Kurt Toman, April 1964 (REPRINT).*
- No. 11. Radiation Forces in Inhomogeneous Media, *E.J. Post, April 1964 (REPRINT).*
- No. 12. Progressive Failure Prediction, *Walton B. Bishop, April 1964 (REPRINT).*
- No. 13. Visual Data Transmission, *Ronald J. Massa, 1/Lt, USAF, April 1964.*
- No. 14. Rydberg Absorption Series of N_2 , *M. Ogawa and Y. Tanaka, May 1964 (REPRINT).*
- No. 15. 600-A Band of Helium, *Y. Tanaka and K. Yoshino, May 1964 (REPRINT).*
- No. 16. Charge Transfer Studies With a Time-of-Flight Mass Spectrometer: II. Kinetic Analysis, Including Attenuation of Both Neutrals and Ions by Scattering, *W. W. Hunt, Jr., May 1964.*
- No. 17. Photo-Induced Electron Transfer in Dye-Sulphydryl Protein Complex, *Eiji Fujimori, May 1964, (REPRINT).*
- No. 18. Intelligibility of Excerpts From Fluent Speech: Auditory vs. Structural Context, *Irwin Pollack and J.M. Pickett, May 1964, (REPRINT).*
- No. 19. A Study of Transverse Modes of Ruby Lasers Using Beat Frequency Detection and Fast Photography, *C. Martin Stickley, May 1964.*
- No. 20. Some Effects of Semantic and Grammatical Context on the Production and Perception of Speech, *Philip Lieberman, June 1964 (REPRINT).*
- No. 21. Infrared Absorption of Magnesium Stannide, *Herbert G. Lipson and Alfred Kahan, June 1964 (REPRINT).*
- No. 22. On the Optimum Design of Multipath Signals, *Neil J. Bershad, 1/Lt USAF, June 1964.*
- No. 23. Area Properties of Television Pictures, *S. Nishikawa, R.J. Massa, J.C. Mott-Smith, June 1964.*
- No. 24. A Geometric Study of Coherence Properties of Partially Polarized Electromagnetic Radiation, *G.F. Bolinder, June 1964.*
- No. 25. The Preparation of High-Purity Boron via the Iodide, *A.F. Armington, G.F. Dillon, and R.F. Mitchell, June 1964 (REPRINT).*
- No. 26. An Interpretation of the Far-Field Effects of a Rocket in the Ionosphere (U), *Thomas D. Conley and James E. Piggins, June 1964 (SECRET).*
- No. 27. A Radon-Nikodym Theorem in Dimension Lattices, *S.S. Holland, Jr., June 1964 (REPRINT).*
- No. 28. Plasma Produced Antenna Pattern Distortion, *Daniel J. Jacavano, June 1964.*
- No. 29. Geometry and First-Order Error Statistics for Three- and Four-Station Hyperbolic Fixes on a Spherical Earth, *Edward A. Lewis, June 1964.*
- No. 30. Ion Dissociation in the Drift Tube of a Time-of-Flight Mass Spectrometer: III Flight-Time Shift Equations for Spurious Fragment Peaks Arising From Charge Transfer and Dissociation Reactions Occurring Inside the Potential Barrier, *W.W. Hunt, Jr., June 1964.*
- No. 31. Dolph Chebyscheff Arrays of Many Elements and Arbitrary Uniform Spacing, *Charles J. Drane, Jr., June 1964.*

PHYSICAL SCIENCES RESEARCH PAPERS (Continued)

- No. 32. Measurement of Noise Figure of an λ -Band Waveguide Mixer with Tunnel Diode, *Gustav H. Blaeser*, July 1964.
- No. 33. Transient Reflection and Transmission of a Plane Wave Normally Incident Upon a Semi-Infinite Anisotropic Plasma, *Carl T. Case, 1/Lt, USAF*, July 1964.
- No. 34. Low-Temperature Far-Infrared Spectra of Germanium and Silicon, *Peter J. Gielisse, James R. Aronson and Hugh G. McLinden*, June 1964.
- No. 35. Absorption Coefficients of Carbon Monoxide in the 1006-600-A Wavelength Region, *R.E. Huffman, J.C. Larrabee and Y. Tanaka*, July 1964. (REPRINT).
- No. 36. Asymptotic Form of the Electron Capture Cross Section in First Born and Distorted Wave Approximations, *R.A. Mapleton*, July 1964. (REPRINT).
- No. 37. A Computer Approach to Laser Design, *T.G. Purnhagen and J. Lubelfeld*, July 1964. (REPRINT).
- No. 38. Apparent Sky Temperatures at Millimeter-Wave Frequencies, *Karl N. Fulsberg*, July 1964.